Journal of Computational Physics **170,** 676–695 (2001)
doi:10.1006/jcph.2001.6756, available online at http://www.idealibrary.com on IDEAL®

Wave Simulation in Frozen Porous Media

José M. Carcione and Géza Seriani

Istituto Nazionale di Oceanografia e di Geofisica Sperimentale (OGS), Borgo Grotta Gigante 42c, 34010 Sgonico, Trieste, Italy
E-mail: jcarcione@ogs.trieste.it; gseriani@ogs.trieste.it

Received May 12, 2000; revised February 2, 2001

We propose a numerical algorithm for simulation of wave propagation in frozen porous media, where the pore space is filled with ice and water. The model, based on a Biot-type three-phase theory, predicts three compressional waves and two shear waves and models the attenuation level observed in rocks. Attenuation is modeled with exponential relaxation functions which allow a differential formulation based on memory variables. The wavefield is obtained using a grid method based on the Fourier differential operator and a Runge–Kutta time-integration algorithm. Since the presence of slow quasistatic modes makes the differential equations stiff, a time-splitting integration algorithm is used to solve the stiff part analytically. The modeling is second-order accurate in the time discretization and has spectral accuracy in the calculation of the spatial derivatives.

Key Words: wave simulation; frozen porous media; Biot-type theory; poroviscoelasticity.

1. INTRODUCTION

Knowledge of the physical properties of frozen soils is essential for the exploitation of mineral resources in polar areas and quantification of the amount of drilling necessary for the construction of highways and pipelines. Another recent application concerns bottom simulating reflectors (BSR), which are shallow seismic anomalies caused by gas-hydrate sediments trapping underlying free gas-bearing sediments partially saturated with water. These applications require the knowledge of the degree of freezing of the interstitial water. Freezing has a negligible effect on density and magnetic permeability, precluding the use of gravimetric and magnetic techniques, but have a remarkable effect on wave velocities (see Timur [24], Carcione and Seriani [7]). Hence, seismic and acoustic logging methods constitute the best way for quantifying the amount of ice and water.

A Biot-type three-phase theory based on first principles has been recently proposed by Leclaire *et al*. [17]. The theory, which assumes that there is no direct contact between solid

0021-9991/01 $35.00

grains (rock frame) and ice, predicts three compressional waves and two shear waves and can be applied to unconsolidated and consolidated media. Leclaire *et al.* [17] also provide a thermodynamic relation between water proportion and temperature. Here, we generalize the theory to include grain–ice interaction and grain cementation with decreasing temperature and provide an explicit relation between water proportion and temperature. Moreover, it is well known that Biot-type theories do not appropriately model the levels of wave attenuation observed in rocks [19]. Gurevich *et al.* [12] performed experiments on a sample made of sintered glass beads and used Biot's pore form factor as a fitting parameter to model the amplitudes. This factor controls the behavior of the dynamic permeability/tortuosity function. However, although this approach successfully describes the wave propagation properties of synthetic porous media such as sintered glass beads, in natural porous media such as sandstone, discrepancies between Biot theory and measurements are due to complex pore shapes and the presence of clay, which are not present in synthetic media. This complexity gives rise to a variety of relaxation mechanisms that contribute to the attenuation of the different wave modes. Stoll and Bryan [23] show that attenuation is controlled by the anelasticity of the skeleton (friction at grain contacts and interaction with the fluid) and by viscodynamic causes. Thus, we model realistic attenuation levels by generalizing the elastic moduli to time-dependent relaxation functions, which implies the introduction of additional differential equations [3].

The Lagrangian formulation used by Leclaire *et al.* [17] holds for uniform porosity, since they use the average displacements of the solid and fluid phases as Lagrangian coordinates and the respective stress components as conjugate variables. In a two-phase porous medium with non-uniform porosity, Biot [2] proposes as generalized coordinates the displacements of the solid matrix and the variation of fluid content. In this case the corresponding conjugate variables are the total stress components and the fluid pressure.

Biot's poroviscoelastic differential equations have the form $\dot{\mathbf{w}} = \mathbf{M}\mathbf{w}$, where $\mathbf{w}$ is the wavefield vector and $\mathbf{M}$ is the propagation matrix (the dot denotes time differentiation). As in the poroacoustic case [6], all the eigenvalues of $\mathbf{M}$ have negative real part. While the eigenvalues of the fast waves have a small real part, the eigenvalues of the slow waves (in the quasi-static regime) have a large real part. The presence of these quasi-static modes makes the differential equations *stiff* [14]. Thus, seismic and sonic modeling are unstable when using explicit time integration methods. Carcione and Quiroga-Goode [6], in the poroacoustic case, and Carcione [4], in the poroelastic case, solved this problem by using a splitting or partition method. The propagation matrix can be partitioned into a stiff part and a non-stiff part as $\mathbf{M} = \mathbf{M}_r + \mathbf{M}_s$, where r indicates the regular matrix and s the stiff matrix. The stiff part is solved analytically and the non-stiff part is solved using a standard explicit method. Snapshots and time histories are obtained by solving the equations of motion with a direct grid algorithm based on the Fourier pseudospectral method for computing the spatial derivatives (e.g., Carcione [4]). An example of wave propagation in a partially frozen sandstone illustrates the potentialities of the theory and simulation algorithm.

2. EQUATIONS OF MOTION

In this section we obtain the velocity–stress formulation for 2-D wave propagation in a frozen porous medium that may represent an ice- (or gas-hydrate)-bearing rock. Leclaire *et al.* [17] assume that there is no direct contact between solid and ice. Here we have included this contribution to the potential and kinetic energies, and the stiffening of the rock frame

resulting from grain cementation by ice at freezing temperatures. More details can be found in Carcione and Tinivella [8].

2.1. *Conservation of Momentum*

The equations of momentum conservation are deduced using Lagrange's equations. Substituting the generalized momenta (10) in [17] into Lagrange's equations (13) in [17] yields

$$\begin{aligned}
\sigma^{(1)}_{ix,x} + \sigma^{(1)}_{iz,z} &= \rho_{11}\dot{v}^{(1)}_i + \rho_{12}\dot{v}^{(2)}_i + \rho_{13}\dot{v}^{(3)}_i - b_{12}\left(v^{(2)}_i - v^{(1)}_i\right) - b_{13}\left(v^{(3)}_i - v^{(1)}_i\right),\\
\sigma^{(2)}_{,i} &= \rho_{12}\dot{v}^{(1)}_i + \rho_{22}\dot{v}^{(2)}_i + \rho_{23}\dot{v}^{(3)}_i + b_{12}\left(v^{(2)}_i - v^{(1)}_i\right) + b_{23}\left(v^{(2)}_i - v^{(3)}_i\right), \quad (1)\\
\sigma^{(3)}_{ix,x} + \sigma^{(3)}_{iz,z} &= \rho_{13}\dot{v}^{(1)}_i + \rho_{23}\dot{v}^{(2)}_i + \rho_{33}\dot{v}^{(3)}_i - b_{23}\left(v^{(2)}_i - v^{(3)}_i\right) + b_{13}\left(v^{(3)}_i - v^{(1)}_i\right),
\end{aligned}$$

where subscript i represents x or z, the σ's are stress components, and the v's are particle velocities. The superscripts 1, 2, and 3 refer to solid grain, water, and ice, respectively, a dot above a variable denotes time differentiation, and spatial derivatives with respect to a variable y are indicated by the subscript, "y". The friction terms in Eq. (1) have signs opposite to those given in [17], otherwise the equations are physically unstable (wave amplitude increases with time). The signs here coincide with those of Biot's differential equations (see Refs. [2, 4]) in the limit of full water saturation. The choice of the correct signs can be based, for instance, on the signs of the eigenvalues of matrix **S**. They should be negative to obtain attenuating solutions (see Eqs. (23) and (24)). Details of the material properties are given in Appendix A.

The expressions for the density components, given in Appendix A, include the interaction between the grains and the ice, assuming that the grains flow through the ice matrix (described by the tortuosity a_{13}) and the ice flows through the rock frame (described by a_{31}). As is well known, the tortuosity is related to the difference between the microvelocity and macrovelocity fields. If they are similar (i.e., for relatively rigid materials such as solids), the tortuosities equal 1 and the contributions vanish. However, we assume that these terms contribute to the kinetic energy when the solid and ice matrices are unconsolidated or relatively unconsolidated, for which the tortuosities are greater than 1. As in the Biot theory, we neglect the contributions due to the interaction between the solid phases and water (related to the tortuosity a_{12} and a_{32}).

2.2. *Stress–Strain Relations*

The 2-D constitutive equations are given by Eqs. (7) of [17], with the addition of the terms corresponding to grain–ice interaction in the potential energy. Using the notation in [17], these terms are $C_{13}\theta_1\theta_3$ and $\mu_{13}d^{(1)}_{ij}d^{(3)}_{ij}$. We obtain

$$\begin{aligned}
\sigma^{(1)}_{xx} &= (K_1+\mu_1)\epsilon^{(1)}_{xx} + (K_1-\mu_1)\epsilon^{(1)}_{zz} + C_{12}\theta_2 + (C_{13}+\tfrac{1}{2}\mu_{13})\epsilon^{(3)}_{xx} + (C_{13}-\tfrac{1}{2}\mu_{13})\epsilon^{(3)}_{zz},\\
\sigma^{(1)}_{zz} &= (K_1+\mu_1)\epsilon^{(1)}_{zz} + (K_1-\mu_1)\epsilon^{(1)}_{xx} + C_{12}\theta_2 + (C_{13}+\tfrac{1}{2}\mu_{13})\epsilon^{(3)}_{zz} + (C_{13}-\tfrac{1}{2}\mu_{13})\epsilon^{(3)}_{xx},\\
\sigma^{(1)}_{xz} &= 2\mu_1\epsilon^{(1)}_{xz} + \mu_{13}\epsilon^{(3)}_{xz},\\
\sigma^{(2)} &= C_{12}\left(\epsilon^{(1)}_{xx} + \epsilon^{(1)}_{zz}\right) + K_2\theta_2 + C_{23}\left(\epsilon^{(3)}_{xx} + \epsilon^{(3)}_{zz}\right),
\end{aligned}$$

$$\begin{aligned}
\sigma_{xx}^{(3)} &= (K_3+\mu_3)\epsilon_{xx}^{(3)} + (K_3-\mu_3)\epsilon_{zz}^{(3)} + C_{23}\theta_2 + (C_{13}+\tfrac{1}{2}\mu_{13})\epsilon_{xx}^{(1)} + (C_{13}-\tfrac{1}{2}\mu_{13})\epsilon_{zz}^{(1)},\\
\sigma_{zz}^{(3)} &= (K_3+\mu_3)\epsilon_{zz}^{(3)} + (K_3-\mu_3)\epsilon_{xx}^{(3)} + C_{23}\theta_2 + (C_{13}+\tfrac{1}{2}\mu_{13})\epsilon_{zz}^{(1)} + (C_{13}-\tfrac{1}{2}\mu_{13})\epsilon_{xx}^{(1)},\\
\sigma_{xz}^{(3)} &= 2\mu_3\epsilon_{xz}^{(3)} + \mu_{13}\epsilon_{xz}^{(1)},\\
\theta_2 &= \epsilon_{xx}^{(2)} + \epsilon_{zz}^{(2)},
\end{aligned} \tag{2}$$

where the ϵ's are the usual strain components [21]. The expressions for K_{max} and μ_{max} (see Appendix A) can be found in Zimmerman and King [27, Eqs. (1) and (2), respectively], with the subscript m denotes ice, i denotes air, and the concentration c is equal to ϕ_s. They are the moduli of the ice matrix, with the water totally frozen and the solid replaced by air. However, we assume that the rigidity modulus of the rock frame μ_{sm} is affected by the cementation of the sand grains with ice. The equation, indicated in Appendix A, follows the same percolation model used for the ice matrix [17]. The rigidity μ_{smKT} is the Kuster and Toksöz shear modulus of the rock frame with air as inclusion, with a concentration $1-\phi_s$.

A very thin and viscous water layer may transmit, depending on the frequency, shear deformations from one matrix to the other. In this case, the coefficients μ_1, μ_2, and μ_{13} become relaxation functions and should be replaced by the operators μ_1*, μ_2*, and $\mu_{13}*$ ($*$ denotes time convolution), with μ_{av} representing a Maxwell mechanical model with two springs, whose stiffnesses are $\mu_s/(1-g_1)\phi_s$ and $\mu_i/(1-g_3)\phi_i$, and a dashpot of viscosity η_w/ϕ_w. The use of relaxation function requires the introduction of memory variables and eight additional first-order differential equations [3]. Note that in [17], first the imaginary part of the Maxwell complex modulus is neglected, and then, the related attenuation effects. The additional differential equations are avoided here by using this approximation, i.e., replacing $i\omega\eta$ by $2\omega\eta$ in μ_{av} and taking ω equal to the dominant frequency of the source.

The 3-D constitutive equations can be obtained by including the stress and strain components corresponding to the third dimension (see Leclaire *et al.* [17]) and replacing the coefficients $K_1+\mu_1$ and $K_1-\mu_1$ in Eq. (2) by $K_1+4\mu_1/3$ and $K_1-2\mu_1/3$, respectively. Similarly, $C_{13}+\mu_{13}/2$ and $C_{13}-\mu_{13}/2$ are replaced by $C_{13}+2\mu_{13}/3$ and $C_{13}-\mu_{13}/3$, respectively.

2.3. *Velocity–Stress Formulation*

The velocity–stress formulations are first-order (in the space and time variables) differential equations, where the unknown variables are the particle velocities and stress components. The equations of momentum conservation can be rewritten as

$$\begin{aligned}
\dot{v}_i^{(1)} &= \gamma_{11}\Pi_i^{(1)} + \gamma_{12}\Pi_i^{(2)} + \gamma_{13}\Pi_i^{(3)},\\
\dot{v}_i^{(2)} &= \gamma_{12}\Pi_i^{(1)} + \gamma_{22}\Pi_i^{(2)} + \gamma_{23}\Pi_i^{(3)},\\
\dot{v}_i^{(3)} &= \gamma_{13}\Pi_i^{(1)} + \gamma_{23}\Pi_i^{(2)} + \gamma_{33}\Pi_i^{(3)},
\end{aligned} \tag{3}$$

where

$$\begin{aligned}
\Pi_i^{(1)} &= \sigma_{ix,x}^{(1)} + \sigma_{iz,z}^{(1)} + b_{12}\big(v_i^{(2)} - v_i^{(1)}\big) + b_{13}\big(v_i^{(3)} - v_i^{(1)}\big),\\
\Pi_i^{(2)} &= \sigma_{,i}^{(2)} - b_{12}\big(v_i^{(2)} - v_i^{(1)}\big) - b_{23}\big(v_i^{(2)} - v_i^{(3)}\big),\\
\Pi_i^{(3)} &= \sigma_{ix,x}^{(3)} + \sigma_{iz,z}^{(3)} + b_{23}\big(v_i^{(2)} - v_i^{(3)}\big) - b_{13}\big(v_i^{(3)} - v_i^{(1)}\big)
\end{aligned} \tag{4}$$

are the rate of generalized momenta and γ_{nm} are the components of the symmetric matrix

$$\begin{pmatrix} \rho_{11} & \rho_{12} & \rho_{13} \\ \rho_{12} & \rho_{22} & \rho_{23} \\ \rho_{13} & \rho_{23} & \rho_{33} \end{pmatrix}^{-1}. \tag{5}$$

The equations corresponding to the stress components are obtained by differentiating Eqs. (2) and noting that the rate of the strain components is [21]

$$\dot{\epsilon}_{ij}^{(m)} = \frac{1}{2}\left(v_{i,j}^{(m)} + v_{j,i}^{(m)}\right),$$

with $m = 1, 2, 3$.

2.4. *Extension to the Poroviscoelastic Case*

Wave velocities are generally expected to be lower at low frequencies, typical of seismic measurements, than at high frequencies, typical of laboratory experiments. Since the magnitude of this effect cannot be entirely described by Biot-type theories [19], additional relaxation mechanisms are required to model the velocity dispersion. Measurements of dry-rock velocities contain all the information about pore shapes and pore interactions, and their influence on wave propagation. Low-frequency wet rock velocities can be calculated by using the equivalent of the Gassmann relations of the three-phase theory, i.e., the low-frequency limit of the dispersion relation [5, 10]. High-frequency wet-rock velocities are then given by the unrelaxed velocities. Since dry-rock velocities are practically frequency independent, the data can be obtained from laboratory measurements.

Viscoelasticity is introduced into the poroelastic equations for modeling a variety of dissipation mechanisms. One of these mechanisms is the squirt flow [2, 20] by which a force applied to the area of contact between two grains produces a displacement of the surrounding fluid in and out of this area. Since the fluid is viscous, the motion is not instantaneous and energy dissipation occurs.

We generalize the effective moduli of the rock frame, K_1 and μ_1, and the ice matrix, K_3 and μ_3, to time-dependent relaxation functions and assume that the other coefficients in the potential energy are frequency independent. The following terms in Eq. (2) are considered, $K_m\zeta^{(m)}$, $\mu_m\xi^{(m)}$, and $\mu_m\epsilon_{xz}^{(m)}$, where $\zeta^{(m)} = \epsilon_{xx}^{(m)} + \epsilon_{zz}^{(m)}$ and $\xi^{(m)} = \epsilon_{xx}^{(m)} - \epsilon_{zz}^{(m)}$, $m = 1, 3$. Denoting, in general, these terms by $M\epsilon$, $M\epsilon$ is replaced by $\psi * \epsilon_{,t}$ in the viscoelastic case, where

$$\psi(t) = M\left(1 + \frac{1}{L}\sum_{l=1}^{L}\varphi_l\right)^{-1}\left[1 + \frac{1}{L}\sum_{l=1}^{L}\varphi_l \exp(-t/\tau_{\sigma l})\right] H(t), \tag{6}$$

with $H(t)$ the Heaviside function,

$$\varphi_l = \frac{\tau_{\epsilon l}}{\tau_{\sigma l}} - 1, \tag{7}$$

and $\tau_{\epsilon l}$ and $\tau_{\sigma l}$ are sets of relaxation times. Equation (6) corresponds to a parallel connection of standard linear solid elements. For high frequencies $(t = 0^+)\psi = M$.

As in the single-phase viscoelastic case [3], we introduce memory variables to avoid the time convolutions. This approach implies the substitution

$$M\epsilon \rightarrow M\epsilon + \sum_{l=1}^{L} e_l,$$

where e_l, $l = 1, \ldots, L$, are the memory variables, which satisfy

$$e_{l,t} = -\frac{1}{\tau_{\sigma l}} \left[M \left(L + \sum_{m=1}^{L} \varphi_m \right)^{-1} \varphi_l \epsilon + e_l \right]. \tag{8}$$

The calculation of the phase velocity and attenuation factor requires a Fourier transformation of the constitutive equations to the frequency domain, which implies the substitution

$$M \rightarrow \bar{M},$$

where

$$\bar{M} = M \left(L + \sum_{l=1}^{L} \varphi_l \right)^{-1} \sum_{l=1}^{L} \frac{1 + i\omega\tau_{\epsilon l}}{1 + i\omega\tau_{\sigma l}}, \tag{9}$$

with ω the angular frequency. The relaxation times can be expressed in terms of a Q-factor Q_l and a reference frequency f_l as

$$\tau_{\epsilon l} = \frac{1}{2\pi f_l Q_l} \left[\sqrt{Q_l^2 + 1} + 1 \right] \tag{10}$$

and

$$\tau_{\sigma l} = \frac{1}{2\pi f_l Q_l} \left[\sqrt{Q_l^2 + 1} - 1 \right]. \tag{11}$$

3. NUMERICAL ALGORITHM

The velocity–stress differential equations can be written in matrix form as

$$\dot{\mathbf{w}} = \mathbf{M}\mathbf{w} + \mathbf{s}, \tag{12}$$

where

$$\mathbf{w} = \left[v_x^{(1)}, v_x^{(2)}, v_x^{(3)}, v_z^{(1)}, v_z^{(2)}, v_z^{(3)}, \sigma_{xx}^{(1)}, \sigma_{zz}^{(1)}, \sigma_{xz}^{(1)}, \sigma^{(2)}, \sigma_{xx}^{(3)}, \sigma_{zz}^{(3)}, \sigma_{xz}^{(3)}, \{e\} \right]^{\top} \tag{13}$$

is the unknown velocity–stress vector, $\{e\}$ represents the set of memory variables,

$$\mathbf{s} = \left[0, 0, 0, 0, 0, 0, s_{xx}^{(1)}, s_{zz}^{(1)}, s_{xz}^{(1)}, s^{(2)}, s_{xx}^{(3)}, s_{zz}^{(3)}, s_{xz}^{(3)}, \{0\} \right]^{\top} \tag{14}$$

is the source vector, and $\mathbf{M}$ is the propagation matrix containing the spatial derivatives and material properties.

For application of the source, we consider three main cases:

1. *Frame sources.* $s^{(2)} = 0$, and the various combinations of $s_{xx}^{(m)}$, $s_{zz}^{(m)}$, and $s_{xz}^{(m)}$ giving a horizontal force, a vertical force, an explosive source, and a pure shear source, all applied to the rock frame ($m = 1$) or to the ice matrix ($m = 3$).
2. *Fluid-volume injection.* The frame sources equal to zero, and $s^{(2)} \neq 0$.
3. *Bulk source.* This case assumes that the energy is partitioned between the three phases and that the shear sources vanish; that is, $s_{xx}^{(1)} = s_{zz}^{(1)} = s^{(2)} = s_{xx}^{(3)} = s_{zz}^{(3)}$.

The solution to Eq. (12) subject to the initial condition $\mathbf{w}(0) = \mathbf{w}_0$ is formally given by

$$\mathbf{w}(t) = \exp(t\mathbf{M})\mathbf{w}_0 + \int_0^t \exp(t'\mathbf{M})\mathbf{s}(t - t')\, dt', \tag{15}$$

where $\exp(t\mathbf{M})$ is called evolution operator.

As in the poroacoustic case [6], the eigenvalues of $\mathbf{M}$ have negative real parts and differ greatly in magnitude because of the terms containing the friction coefficients b_{12} and b_{23}. The presence of large eigenvalues, together with small eigenvalues, indicates that the problem is stiff. The differential equations are solved using the splitting algorithm introduced by Carcione and Quiroga-Goode [6] for two-phase poroacoustic media and by Carcione [4] for two-phase poroelastic media, and generalized here for three-phase porous media. The propagation matrix can be partitioned as

$$\mathbf{M} = \mathbf{M}_r + \mathbf{M}_s, \tag{16}$$

where subscript r indicates the regular matrix and subscript s the stiff matrix. Only the first six differential equations corresponding to the particle velocities in Eq. (3) are stiff. Let us discretize the time variable as $t = ndt$, where dt is the time step. The evolution operator can be expressed as $\exp(\mathbf{M}_r + \mathbf{M}_s)t$. It is easy to show that the product formula

$$\exp(\mathbf{M}\, dt) = \exp\left(\frac{1}{2}\mathbf{M}_s\, dt\right) \exp(\mathbf{M}_r\, dt) \exp\left(\frac{1}{2}\mathbf{M}_s\, dt\right) \tag{17}$$

is second-order accurate in dt (see Gourlay [11] and Vreugdenhil [25]). Equation (17) allows us to solve the stiff part separately. Using the Kronecker product "$\otimes$" of two matrices yields

$$\mathbf{M}_s = \begin{pmatrix} \mathbf{I}_2 \otimes \mathbf{S} & \mathbf{0} \\ \mathbf{0} & \mathbf{0} \end{pmatrix}, \tag{18}$$

where $\mathbf{I}_2$ is the 2×2 identity matrix. We should solve

$$\dot{\mathbf{v}}_i = \mathbf{S}\mathbf{v}_i, \tag{19}$$

for each Cartesian component i, where

$$\mathbf{v}_i = \left[v_i^{(1)}, v_i^{(2)}, v_i^{(3)}\right]^\top, \tag{20}$$

and

$$\mathbf{S}_{11} = b_{12}(\gamma_{12} - \gamma_{11}) + b_{13}(\gamma_{13} - \gamma_{11}),$$
$$\mathbf{S}_{12} = b_{12}(\gamma_{11} - \gamma_{12}) + b_{23}(\gamma_{13} - \gamma_{12}),$$

$$
\begin{aligned}
\mathbf{S}_{13} &= b_{23}(\gamma_{12} - \gamma_{13}) + b_{13}(\gamma_{11} - \gamma_{13}),\\
\mathbf{S}_{21} &= b_{12}(\gamma_{22} - \gamma_{12}) + b_{13}(\gamma_{23} - \gamma_{12}),\\
\mathbf{S}_{22} &= b_{23}(\gamma_{23} - \gamma_{22}) + b_{12}(\gamma_{12} - \gamma_{22}),\\
\mathbf{S}_{23} &= b_{23}(\gamma_{22} - \gamma_{23}) + b_{13}(\gamma_{12} - \gamma_{23}),\\
\mathbf{S}_{31} &= b_{12}(\gamma_{23} - \gamma_{13}) + b_{13}(\gamma_{33} - \gamma_{13}),\\
\mathbf{S}_{32} &= b_{12}(\gamma_{13} - \gamma_{23}) + b_{23}(\gamma_{33} - \gamma_{23}),\\
\mathbf{S}_{33} &= b_{23}(\gamma_{23} - \gamma_{33}) + b_{13}(\gamma_{13} - \gamma_{33}).
\end{aligned}
\tag{21}
$$

The solution of Eq. (19) is

$$
\mathbf{v}_i(\tau) = \exp(\mathbf{S}\tau)\,\mathbf{v}_i(0), \tag{22}
$$

where $\exp(\mathbf{S}\tau)$ can be obtained analytically by solving a set of three recurrent ordinary differential equations [22], which gives

$$
\exp(\mathbf{S}\tau) = \mathbf{I}_3 - \frac{1 - e^{\lambda_1 \tau}}{\lambda_1}\,\mathbf{S} + \frac{\left(1 - e^{\lambda_2 \tau}\right)\lambda_1 - \left(1 - e^{\lambda_1 \tau}\right)\lambda_2}{\lambda_1 \lambda_2 (\lambda_1 - \lambda_2)}\,\mathbf{S} \cdot (\mathbf{S} - \lambda_1 \mathbf{I}_3), \tag{23}
$$

with $\{0,\ \lambda_1,\ \lambda_2\}$ the eigenvalues of matrix $\mathbf{S}$ and $\mathbf{I}_3$ the 3×3 identity matrix. The eigenvalues are

$$
\lambda_1 = \frac{1}{2}[\mathrm{tr}(\mathbf{S}) - \sqrt{[\mathrm{tr}(\mathbf{S})]^2 - 4E}], \qquad \lambda_2 = \mathrm{tr}(\mathbf{S}) - \lambda_1, \tag{24}
$$

where

$$
E = S_{13}S_{21} - S_{11}S_{23} - S_{13}S_{31} + S_{23}S_{31} + S_{11}S_{33} - S_{21}S_{33}.
$$

The regular operator $\exp(\mathbf{M}_r \tau)$ is approximated with a fourth-order Runge–Kutta solver [4]. The output vector is

$$
\mathbf{w}^{n+1} = \mathbf{w}^* + \frac{\tau}{6}(\Delta_1 + 2\Delta_2 + 2\Delta_3 + \Delta_4), \tag{25}
$$

where

$$
\begin{aligned}
\Delta_1 &= \mathbf{M}_r \mathbf{w}^* + \mathbf{s}^n,\\
\Delta_2 &= \mathbf{M}_r \left(\mathbf{w}^* + \tfrac{\tau}{2}\Delta_1\right) + \mathbf{s}^{n+1/2},\\
\Delta_3 &= \mathbf{M}_r \left(\mathbf{w}^* + \tfrac{\tau}{2}\Delta_2\right) + \mathbf{s}^{n+1/2},\\
\Delta_4 &= \mathbf{M}_r (\mathbf{w}^* + \tau\Delta_3) + \mathbf{s}^{n+1},
\end{aligned}
$$

and $\mathbf{w}^*$ is the intermediate output vector obtained after the operation with the stiff evolution operator.

Note that the two operations with (17) implies

$$
\exp(2\mathbf{M}\,dt) = \exp\left(\frac{1}{2}\mathbf{M}_s\,dt\right)\exp(\mathbf{M}_r\,dt)\exp(\mathbf{M}_s\,dt)\exp(\mathbf{M}_r\,dt)\exp\left(\frac{1}{2}\mathbf{M}_s\,dt\right). \tag{26}
$$

TABLE I
Material Properties for Frozen Berea Sandstone

Media	Density (kg/m^3)	Bulk modulus (GPa)	Shear modulus (GPa)	
Grain	$\rho_s = 2650$	$K_s = 38.7$	$\mu_s = 39.6$	$\kappa_{s0} = 1.07 \times 10^{-13}$ m^2
Ice	$\rho_i = 920$	$K_i = 8.58$	$\mu_i = 3.32$	$\kappa_{i0} = 5 \times 10^{-4}$ m^2
Water	$\rho_w = 1000$	$K_w = 2.25$	$\mu_w = 0$	$\eta_w = 1.798$ cP*

*1 cP $= 0.001$ Pa · s.

Then, $n - 1$ stiff operations can be saved in n time steps, if only snapshots of the wavefield at $n\,dt$ are to be computed. Moreover, $n(1 - 1/m)$ stiff operations can be saved when computing seismograms with a sampling rate of m time steps.

The spatial derivatives are calculated with the Fourier method by using the fast Fourier transformation [9]. This approximation is infinitely accurate for bandlimited periodic functions with cutoff spatial wavenumbers which are smaller than the cutoff wavenumbers of the mesh.

4. EXAMPLES

We consider wave propagation in a frozen sandstone with a porosity of 20%. The data (see Table I) correspond to Berea sandstone, with the properties given by Timur [24] and Winkler [26]. Figure 1 shows the water proportion ϕ_w as a function of temperature, computed from Eq. (A.4), assuming that $r_{av} = 10$ μm, $\Delta r = 10$ μm, and $r_0 = 0.04$ μm. At -1°C the water proportion is 10% (50% water saturation and 50% ice saturation). The dry-rock bulk and shear moduli at full water saturation are 14.4 and 13.1 GPa, respectively. By virtue of the percolation model, the rock-frame shear modulus at -1°C is 26.1 GPa. We assume that $a_{13} = a_{31} = 1$ and that there is no friction between the rock frame and ice matrix. It is important to note that the velocities of the slow waves greatly depend on the values of the tortuosities.

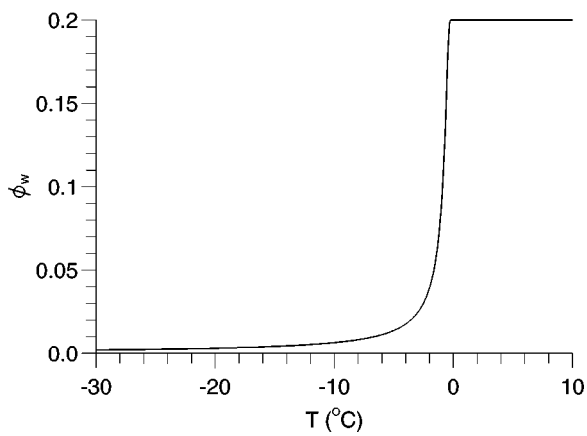

FIG. 1. Water proportion as a function of temperature.

In the first example we assume no losses due to viscoelastic effects. We consider a 357×357 mesh with square cells and a grid spacing of 14 m. The perturbation has a dominant frequency of 12.5 Hz. It is a combination of bulk sources and shear forces in the rock frame and ice matrix, and fluid-volume injection in the fluid. Figure 2 shows the phase velocities of the five wave modes versus water proportion, where the compressional waves are labeled P1, P2, and P3, and the shear waves are labeled S1 and S2. The different pictures correspond to (a) $\eta = 0$, (b) $\eta \neq 0$, and (c) $\eta \neq 0$ and $\kappa_{i0} = \kappa_{s0}$. The first case is unrealistic but allows the verification of the modeling algorithm by calculating the travel times of the different waves (see Fig. 3a). The dots indicate the velocities at 50% water saturation. The values of the velocities are 4124 m/s for P1, 2511 m/s for S1, 1227 m/s for P2, 386 m/s for S2, and 255 m/s for P3. A representation of the curves in Fig. 2b versus the logarithm of ϕ_w shows that the velocities of the P2 and S2 waves are zero at very low water content. At full water saturation three waves propagate, and their velocities are those predicted by Biot's theory. The second case corresponds to realistic values of the rock-frame and ice-matrix permeabilities [17]; one of the slow waves (P3) is quasistatic. In the third case we assume that the ice-matrix permeability equals the rock-frame permeability and show that the other slow waves also become quasistatic modes. This fact may implicitly reflect the presence of clay particles. They reduce both the porosity and the permeability of the rock, and increase the surface area by increasing the attenuation of the slow waves [16]. The attenuation factors (see Appendix A) are between 8 and 60 nepers/m for the quasistatic modes, while those of the propagating waves are between 10^{-9} and 10^{-8} nepers/m; i.e., these waves are lossless in practice.

Snapshots of the wavefield corresponding to the three cases are shown in Figs. 3a, 3b, and 3c. Waves S2 and P3 are aliased, since the mesh "supports" a minimum velocity of 700 m/s according to the Nyquist criterion. As can be appreciated, the snapshots are in agreement with the predictions of the theory. Leclaire *et al.* [18] verified the existence of four of the five waves by performing ultrasonic experiments in water-saturated glass powder (they did not observe the P3 wave). According to Leclaire *et al.* [18], the energy of the P2 and S2 waves propagates mainly in the ice matrix when the medium is almost frozen. Since these waves have low attenuation (at high frequencies, 500 kHz), they consider these waves to be of the first kind. We observe here that these waves become quasistatic when both the rock-frame and the ice-matrix permeabilities are relatively low [case (c)]; otherwise they are propagating waves. On the other hand, the P3 wave is quasistatic when only one of the permeabilities is low.

Figure 4 shows snapshots of the vertical particle velocity at 0.68 ms corresponding to the fluid (a) and ice matrix (b) (the particle velocity of the rockframe is shown in Fig. 3a). The energy of the slow waves P2 and S2 propagates mainly in the ice, as stated in Leclaire *et al.* [18]. The ratio of maximum amplitude in (b) to maximum amplitude in (a) is 276. The situation by which ice grows in a frozen rock, such as Berea sandstone, is probably different from the case observed by Leclaire *et al.* [18] in uncosolidated glass powder. Thus, it is possible that the P2 and S2 waves cannot be observed, in general, in real consolidated rocks.

Johnson [15] has shown that several waves exist in a porous medium under two conditions: (i) the phases have a percolating structure; i.e., it is possible to find a continuous path between two points arbitrarily spaced, and (ii) one of the phases is a fluid. He also studied the case of a solid/solid heterogeneous material and has shown that vibration was not possible at some frequencies. The main reason is that no flow or relative motion of one phase with respect to the other is possible in the solid/solid case. In the present model, we observe the following:

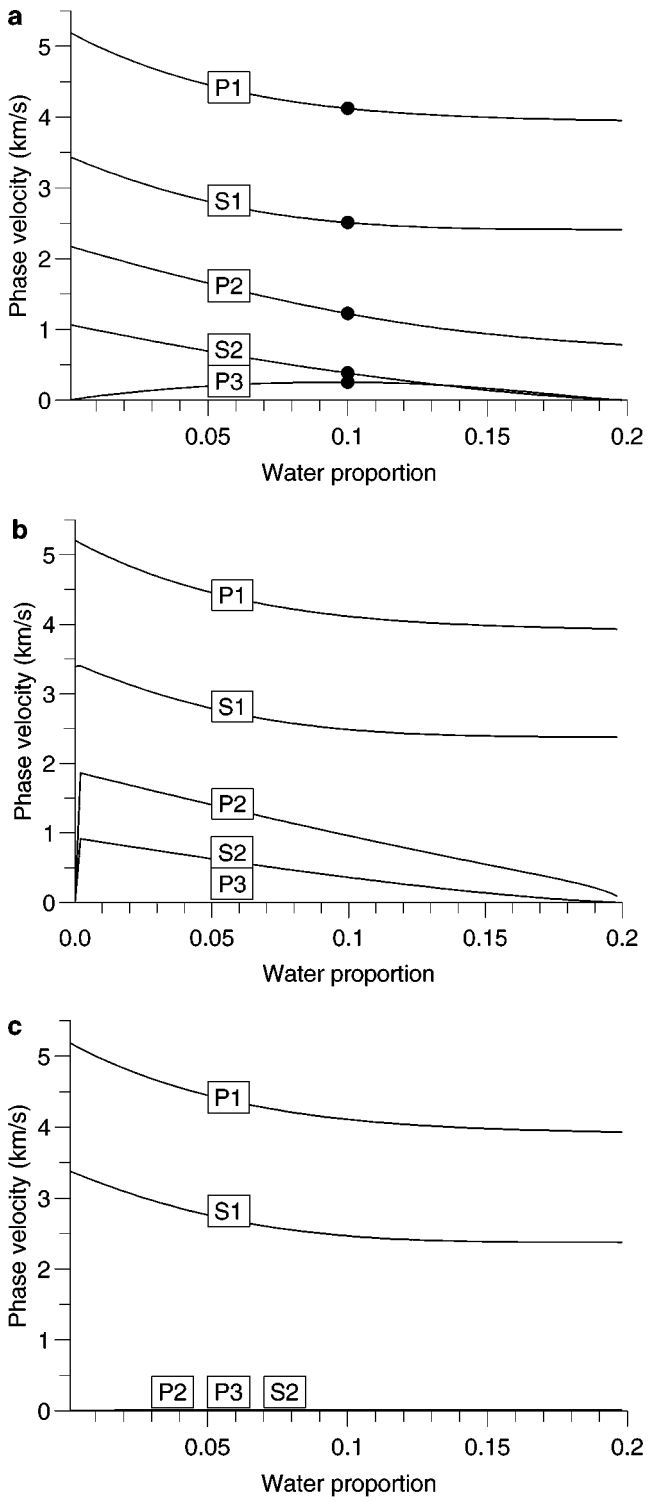

FIG. 2. Phase velocities of the five wave modes propagating in partially frozen Berea sandstone versus water proportion, where (a) corresponds to $\eta = 0$, (b) to $\eta \neq 0$, and (c) to $\eta \neq 0$ and $b_{13} = b_{12}$ ($\kappa_{i0} = \kappa_{s0}$). The compressional waves are labeled P1, P2, and P3, and the shear waves are labeled S1 and S2. The dots indicate the velocities at 50% water saturation, where the values of the velocities are 4124 m/s for P1, 2511 m/s for S1, 1227 m/s for P2, 386 m/s for S2, and 255 m/s for P3.

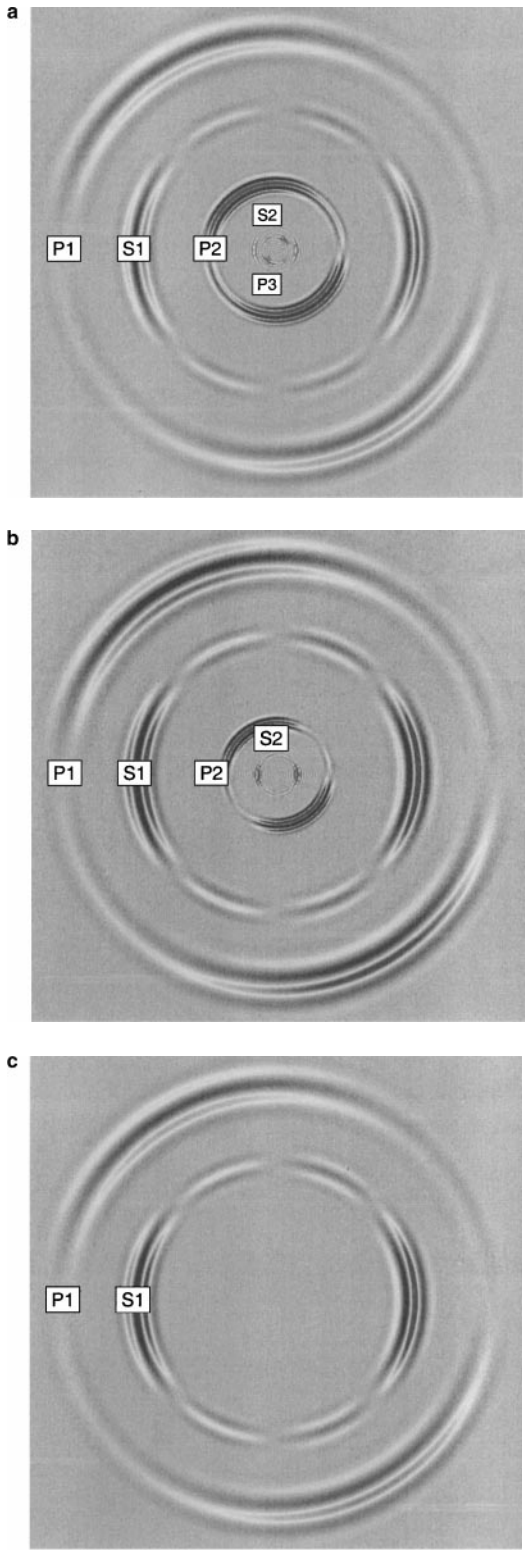

FIG. 3. Snapshots of the rock-frame vertical particle velocity at 0.68 s, corresponding to three cases illustrated in Fig. 2. The mesh has 351 $\times$ 351 grid points and the source is applied at grid point (178, 178). The compressional waves are labeled P1, P2, and P3, and the shear waves are labeled S1 and S2.

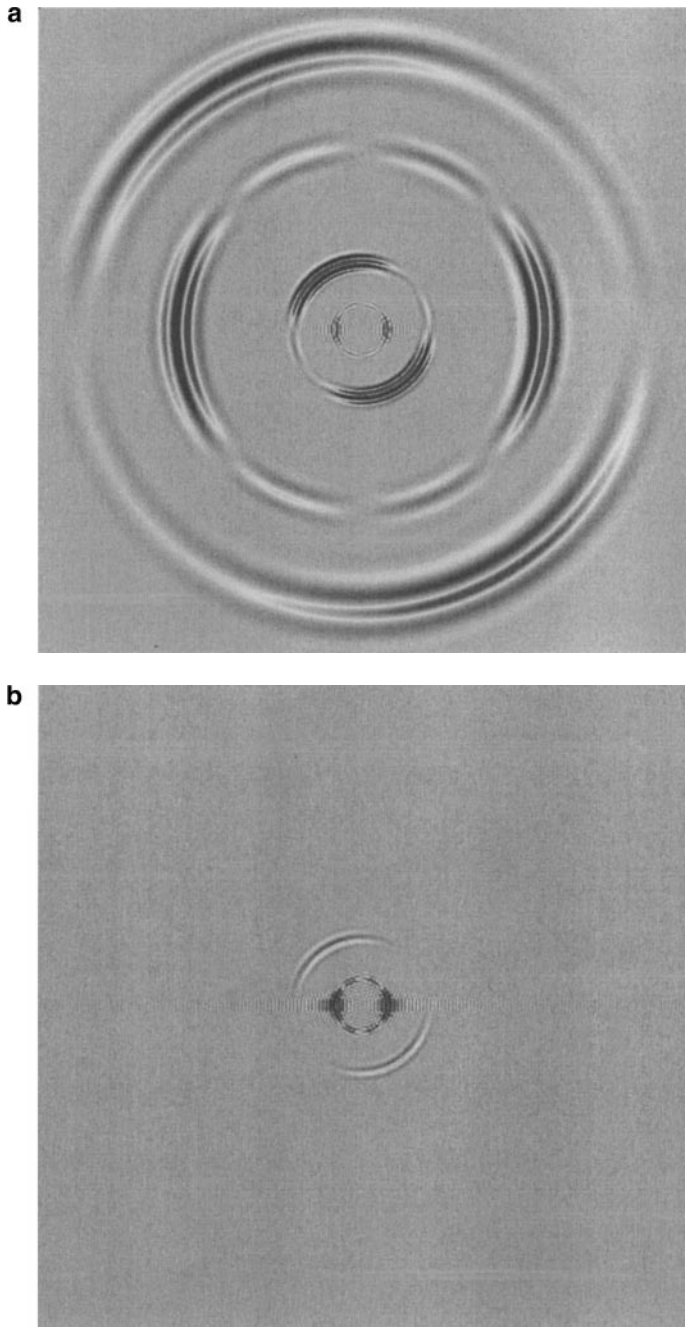

FIG. 4. Snapshots of the vertical particle velocity at 0.68 ms for the fluid (a) and ice matrix (b). The simulation corresponds to case (b) in Fig. 1.

(i) P1 and S1 are the usual body waves which we observe in the acoustics of material media. They correspond to all the phases moving in phase and propagate irrespective of the values of the viscosity and permeabilities.

(ii) P2 is the Biot wave. It is a propagation mode for full water saturation and $b_{12} = 0$ (the case in Fig. 2a, i.e., zero viscosity or infinite rock-frame permeability) and a quasistatic

TABLE II
Phase Velocities and Attenuation Factors

	Poroelastic		Poroviscoelastic	
Wave	V (km/s)	α (neper/km)	V (km/s)	α (neper/km)
P1	4.116	8.5×10^{-6}	4.288	0.36
P2	0.964	1.24×10^{-2}	0.968	0.17
P3	2.5×10^{-3}	31200	2.5×10^{-3}	31200
S1	2.488	8.2×10^{-5}	2.615	0.73
S2	0.363	3.1×10^{-2}	0.363	3.4×10^{-2}

mode for full water saturation and $b_{12} \neq 0$ (assuming realistic values of viscosity and permeability, i.e., the case in Fig. 2b).

(iii) P2 (and S2) is a propagation mode in the presence of ice (excluding $\phi_w = 0$, as mentioned before when discussing Fig. 2b). This means that this mode becomes a wave with increasing freezing and propagates mainly in the ice frame, as predicted by the snapshots in Fig. 4.

(iv) P3 is quasistatic at zero and full water saturations, even in the absence of friction between the phases. This wave could probably be observed in synthetic partially frozen materials and under very particular conditions, e.g., a fluid of negligible viscosity (obviously not water) and a highly permeable porous medium.

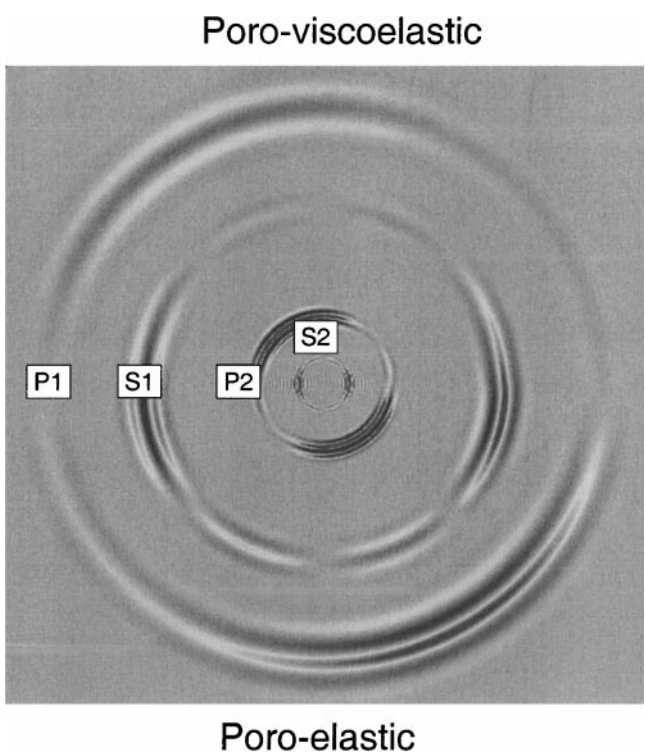

FIG. 5. Snapshot of the rock-frame vertical particle velocity at 0.68 s, where the upper half-space is poro-viscoelastic and the lower half-space is poroelastic. The compressional waves are labeled P1, P2, and P3, and the shear waves are labeled S1 and S2.

(v) The condition of no slow-wave motion in the solid/solid case (the case of a totally frozen medium ($\phi_w = 0$)) is shown in Fig. 2b, i.e., for very low water saturation (the velocities of P2 and S2 vanish at $\phi_w = 0$, as mentioned before). The limiting case $\phi_w = 0$ requires further investigation by recasting the dispersion relation in analytic form.

In the last example we assume that the rock frame is viscoelastic, with one relaxation mechanism ($L = 1$) corresponding to each effective modulus, K_1 and μ_1. The Q-factor parameters in Eqs. (10) and (11) are $Q(K_1) = 30$ and $Q(\mu_1) = 20$, and the reference frequencies are $f(K_1) = f(\mu_1) = 12.5$ Hz. Table II compares the values of the phase velocities and attenuation factors for the poroelastic and poroviscoelastic cases [case (b)]. Rock-frame viscoelasticity mainly affects the waves of the first kind. Figure 5 shows a snapshot of the rock-frame vertical particle velocity at 0.68 s, where the upper half-space is poroviscoelastic and the lower half-space is poroelastic. The attenuation of the P1 and S1 waves in the upper half-space is evident.

5. CONCLUSIONS

We have developed a numerical algorithm for wave simulation in a frozen rock. The differential equations are based on a three-phase Biot-type theory and include viscoelastic effects to describe realistic attenuation values. Low rock-frame and ice-matrix permeabilities make the slow waves quasi-static and the governing equations stiff. They are partitioned into a non-stiff part and a stiff part, which are solved by a standard explicit time-integration algorithm and analytically, respectively. The resulting algorithm is second-order accurate in time and has spectral accuracy in the space variable. The algorithm, which allows general material variability but assumes uniform porosity, provides snapshots and time histories of the rock-frame, ice-matrix, and water particle velocities and corresponding stress components. The differential equations of motion for non-uniform porosity require a careful derivation of the stress–strain relations in terms of the relevant thermodynamic potential. This aspect of the problem will be developed in a forthcoming publication.

APPENDIX A

Theory of Partially Ice- (Gas Hydrate)-Saturated Porous Media

A.1. *List of Symbols*

a_{21}	tortuosity for water flowing through the rock frame
a_{23}	tortuosity for water flowing through the ice matrix
a_{13}	tortuosity for solid grains flowing through the ice matrix
a_{31}	tortuosity for ice flowing through the rock frame
b_{12}	$\eta_w \phi_w^2 / \kappa_s$
b_{13}	friction coefficient between the rock frame and ice matrix
b_{23}	$\eta_w \phi_w^2 / \kappa_i$
c_1	consolidation coefficient for the solid, $c_1 = K_{sm}/\phi_s K_s$
c_3	consolidation coefficient for the ice, $c_3 = K_{im}/\phi_i K_i$
C_{12}	$(1 - c_1)\phi_s \phi_w K_{av}$
C_{13}	$(1 - c_1)(1 - c_3)\phi_s \phi_i K_{av}$
C_{23}	$(1 - c_3)\phi_i \phi_w K_{av}$
f_l	viscoelastic reference frequency

g_1	consolidation coefficient for the solid, $g_1 = \mu_{sm}/\phi_s\mu_s$
g_3	consolidation coefficient for the ice, $g_3 = \mu_{im}/\phi_i\mu_i$
K_s	solid bulk modulus
K_w	water bulk modulus
K_i	ice bulk modulus
K_1	$[(1-c_1)\phi_s]^2 K_{av} + K_{sm}$
K_2	$\phi_w^2 K_{av}$
K_3	$[(1-c_3)\phi_i]^2 K_{av} + K_{im}$
K_{sm}	bulk modulus of the matrix formed by the solid phase
K_{max}	Kuster-Toksöz's bulk modulus for the ice matrix
K_{im}	bulk modulus of the matrix formed by the ice, $K_{im} = K_{max}[\phi_i/(1-\phi_s)]^{3.8}$
K_{av}	average bulk modulus, $K_{av} = [(1-c_1)\phi_s/K_s + \phi_w/K_w + (1-c_3)\phi_i/K_i]^{-1}$
Q_l	Q-factor parameter
r_{21}	geometrical aspect of the boundary separating solid from water
r_{23}	geometrical aspect of the boundary separating ice from water
r_{av}	average radius of the capillary pore
Δr	standard deviation of the capillary pore
η_w	water viscosity
κ_{s0}	rock-frame permeability
κ_{i0}	ice-matrix permeability
κ_s	$\kappa_{s0}\phi_w^3/(1-\phi_s)^3$
κ_i	$\kappa_{i0}[(1-\phi_s)/\phi_i]^2(\phi_w/\phi_s)^3$
μ_s	solid shear modulus
μ_i	ice shear modulus
μ_1	$[(1-g_1)\phi_s]^2\mu_{av} + \mu_{sm}$
μ_{13}	$(1-g_1)(1-g_3)\phi_s\phi_i\mu_{av}$
μ_3	$[(1-g_3)\phi_i]^2\mu_{av} + \mu_{im}$
μ_{smKT}	Kuster–Toksöz's shear modulus for the rock frame
μ_{sm}	rock-frame shear modulus, $\mu_{sm} = [\mu_{smKT} - \mu_{sm0}][\phi_i/(1-\phi_s)]^{3.8} + \mu_{sm0}$
μ_{max}	Kuster–Toksöz's shear modulus for the ice matrix
μ_{im}	shear modulus of the matrix formed by the ice, $\mu_{im} = \mu_{max}[\phi_i/(1-\phi_s)]^{3.8}$
μ_{av}	average shear modulus, $\mu_{av} = [(1-g_1)\phi_s/\mu_s + \phi_w/i\omega\eta_w + (1-g_3)\phi_i/\mu_i]^{-1}$
ω	angular frequency, $\omega = 2\pi f$
ϕ_s	proportion of solid
ϕ_w	proportion of water
ϕ_i	proportion of ice
ρ_s	solid density
ρ_w	water density
ρ_i	ice density
ρ_{11}	$\phi_s\rho_s a_{13} + (a_{21}-1)\phi_w\rho_w + (a_{31}-1)\phi_i\rho_i$
ρ_{12}	$-(a_{21}-1)\phi_w\rho_w$
ρ_{13}	$-(a_{13}-1)\phi_s\rho_s - (a_{31}-1)\phi_i\rho_i$
ρ_{22}	$(a_{21}+a_{23}-1)\phi_w\rho_w$
ρ_{23}	$-(a_{23}-1)\phi_w\rho_w$
ρ_{33}	$\phi_i\rho_i a_{31} + (a_{23}-1)\phi_w\rho_w + (a_{13}-1)\phi_s\rho_s$
$\tau_{\epsilon l}$	viscoelastic relaxation time
$\tau_{\sigma l}$	viscoelastic relaxation time

A.2. *Tortuosities*

Following Berryman [1] and Leclaire *et al.* [17], we express the tortuosity parameters as

$$a_{12} = \frac{\phi_s \rho}{\phi_w \rho_w} r_{12} + 1, \qquad a_{23} = \frac{\phi_i \rho'}{\phi_w \rho_w} r_{23} + 1, \tag{A.1}$$

where

$$\rho = \frac{\phi_w \rho_w + \phi_i \rho_i}{\phi_w + \phi_i}, \qquad \rho' = \frac{\phi_w \rho_w + \phi_s \rho_s}{\phi_w + \phi_s},$$

and $r_{mm'}$ characterize the geometrical features of the pores ($r = 1/2$ for spheres). This approximation is based on the fact that the three phases are mechanically decoupled. Observe that, for instance, $a_{12} \to 1$ for $\phi_w \to 1$ and that $a_{12} \to \infty$ for $\phi_w \to 0$, as expected (see [1]).

By analogy, we may consider that

$$a_{13} = \frac{\phi_i \rho''}{\phi_s \rho_s} r_{13} + 1, \qquad a_{31} = \frac{\phi_s \rho''}{\phi_i \rho_i} r_{31} + 1, \tag{A.2}$$

where

$$\rho'' = \frac{\phi_i \rho_i + \phi_s \rho_s}{\phi_i + \phi_s}.$$

However, this approximation should be used with caution, and it is convenient in most of the cases to use a_{13} and a_{31} as free parameters, as well as the friction coefficient b_{13} between the solid grains and the ice.

A.3. *Water Proportion versus Temperature*

Assuming a Gaussian porosimetric distribution, the water proportion ϕ_w can be obtained as a function of temperature as

$$\phi_w = (1 - \phi_s) A \int_0^{r_0/\ln(T_0/T)} \exp[-(r - r_{av})^2/(2\Delta r^2)] dr, \tag{A.3}$$

where r_{av} is the average pore radius, Δr is the standard deviation, T is the temperature given in Kelvin, and $T_0 = 273$ K [13, 17]. The quantity $r_0 = 0.228$ nm in the ideal case, but here it is used as a parameter to take into account the salinity content of the pore water. As stated by Timur [24], as the ice crystallizes out as pure H_2O, the sodium chloride concentration of the remaining solution increases, thereby further lowering the freezing point. Hence, ice may be thought of as forming on the walls of the larger pores and growing into the pore spaces. This effect is modeled by Eq. (A.3).

The constant A is obtained after normalization of the Gaussian probability function from $r = 0$ to $r = \infty$. Thus, we obtain

$$\phi_w = (1 - \phi_s) \frac{\mathrm{erf}(\zeta) + \mathrm{erf}(\eta)}{1 + \mathrm{erf}(\eta)}, \quad \zeta = \frac{r_0/\ln(T_0/T)}{\sqrt{2}\Delta r} - \eta, \quad \eta = \frac{r_{av}}{\sqrt{2}\Delta r}. \tag{A.4}$$

APPENDIX B

Phase Velocities and Attenuation Factors

The calculation of the phase velocities and attenuation factors follows the approach in [17] and is valid for the 2-D and 3-D cases. The three compressional velocities are given by

$$V_{Pi} = [\mathrm{Re}(\sqrt{\Lambda_i})]^{-1}, \quad i = 1, \ldots, 3, \tag{B.1}$$

where Re takes the real part and Λ_i are obtained from the following characteristic equation:

$$\Lambda^3 \det(\mathbf{R}) - \Lambda^2 a + \Lambda b - \det(\tilde{\boldsymbol{\rho}}) = 0,$$

$$\begin{aligned}
\det(\mathbf{R}) &= R_{11}R_{22}R_{33} - R_{23}^2R_{11} - R_{12}^2R_{33} - R_{13}^2R_{22} + 2R_{12}R_{23}R_{13},\\
a &= a_1 + a_2 + a_3,\\
a_1 &= \tilde{\rho}_{11}\det(R_{iw}) + \tilde{\rho}_{22}\det(R_{si}) + \tilde{\rho}_{33}\det(R_{sw}),\\
a_2 &= -2(\tilde{\rho}_{23}R_{23}R_{11} + \tilde{\rho}_{12}R_{12}R_{33} + \tilde{\rho}_{13}R_{13}R_{22}),\\
a_3 &= 2(\tilde{\rho}_{23}R_{13}R_{12} + \tilde{\rho}_{13}R_{12}R_{23} + \tilde{\rho}_{12}R_{23}R_{13}),\\
\det(R_{sw}) &= R_{11}R_{22} - R_{12}^2,\\
\det(R_{iw}) &= R_{22}R_{33} - R_{23}^2,\\
\det(R_{si}) &= R_{11}R_{33} - R_{13}^2,\\
\det(\tilde{\boldsymbol{\rho}}) &= \tilde{\rho}_{11}\tilde{\rho}_{22}\tilde{\rho}_{33} - \tilde{\rho}_{23}^2\tilde{\rho}_{11} - \tilde{\rho}_{12}^2\tilde{\rho}_{33} - \tilde{\rho}_{13}^2\tilde{\rho}_{22} + 2\tilde{\rho}_{12}\tilde{\rho}_{23}\tilde{\rho}_{13},\\
\det(\rho_{sw}) &= \tilde{\rho}_{11}\tilde{\rho}_{22} - \tilde{\rho}_{12}^2,\\
\det(\rho_{iw}) &= \tilde{\rho}_{22}\tilde{\rho}_{33} - \tilde{\rho}_{23}^2,\\
\det(\rho_{si}) &= \tilde{\rho}_{11}\tilde{\rho}_{33} - \tilde{\rho}_{13}^2,\\
b &= b_1 + b_2 + b_3,\\
b_1 &= R_{11}\det(\rho_{iw}) + R_{22}\det(\rho_{si}) + R_{33}\det(\rho_{sw}),\\
b_2 &= -2(R_{23}\tilde{\rho}_{23}\tilde{\rho}_{11} + R_{12}\tilde{\rho}_{12}\tilde{\rho}_{33} + R_{13}\tilde{\rho}_{13}\tilde{\rho}_{22}),\\
b_3 &= 2(R_{23}\tilde{\rho}_{13}\tilde{\rho}_{12} + R_{13}\tilde{\rho}_{12}\tilde{\rho}_{23} + R_{12}\tilde{\rho}_{23}\tilde{\rho}_{13}).
\end{aligned}$$

Moreover, the two shear velocities V_{Si} are given by

$$V_{Si} = [\mathrm{Re}(\sqrt{\Omega_i})]^{-1}, \quad i = 1, 2, \tag{B.2}$$

where Ω_i are the complex solutions of the equation

$$\begin{aligned}
&\Omega^2 a' - \Omega b' + \det(\tilde{\boldsymbol{\rho}}) = 0,\\
&a' = \tilde{\rho}_{22}\det(\mu_{si}),\\
&b' = \mu_1\det(\rho_{iw}) + \mu_3\det(\rho_{sw}) - 2\mu_{13}\tilde{\rho}_{13}\tilde{\rho}_{22} + 2\mu_{13}\tilde{\rho}_{12}\tilde{\rho}_{23},\\
&\det(\mu_{si}) = \mu_1\mu_3 - \mu_{13}^2.
\end{aligned}$$

The stiffness matrix is given by

$$\mathbf{R} \equiv \begin{pmatrix} R_{11} & R_{12} & R_{13} \\ R_{12} & R_{22} & R_{23} \\ R_{13} & R_{23} & R_{33} \end{pmatrix} = \begin{pmatrix} \bar{K}_1 + n\bar{\mu}_1 & C_{12} & C_{13} \\ C_{12} & K_2 & C_{23} \\ C_{13} & C_{23} & \bar{K}_3 + n\bar{\mu}_3 \end{pmatrix},$$

where $n = 1$ (2-D case) or $n = 4/3$ (3-D case) and the bar indicates the complex viscoelastic modulus. The mass density matrix is

$$\tilde{\boldsymbol{\rho}} \equiv \begin{pmatrix} \tilde{\rho}_{11} & \tilde{\rho}_{12} & \tilde{\rho}_{13} \\ \tilde{\rho}_{12} & \tilde{\rho}_{22} & \tilde{\rho}_{23} \\ \tilde{\rho}_{13} & \tilde{\rho}_{23} & \tilde{\rho}_{33} \end{pmatrix}$$

$$= \begin{pmatrix} \rho_{11} - i(b_{12} + b_{13})/\omega & \rho_{12} + ib_{12}/\omega & \rho_{13} + ib_{13}/\omega \\ \rho_{12} + ib_{12}/\omega & \rho_{22} - i(b_{12} + b_{23})/\omega & \rho_{23} + ib_{23}/\omega \\ \rho_{13} + ib_{13}/\omega & \rho_{23} + ib_{23}/\omega & \rho_{33} - i(b_{23} + b_{13})/\omega \end{pmatrix}.$$

The P-wave and S-wave attenuation factors are given by

$$\alpha_{Pi} = -\omega \mathrm{Im}(\sqrt{\Lambda_i}), \quad i = 1, 2, 3 \tag{B.3}$$

and

$$\alpha_{Si} = -\omega \mathrm{Im}(\sqrt{\Omega_i}), \quad i = 1, 2 \tag{B.4}$$

REFERENCES

1. J. G. Berryman, Confirmation of Biot's theory, *Appl. Phys. Lett.* **37**, 382 (1980).
2. M. A. Biot, Mechanics of deformation and acoustic propagation in porous media, *J. Appl. Phys.* **33**, 1482 (1962).
3. J. M. Carcione, Constitutive model and wave equations for linear, viscoelastic, anisotropic media, *Geophysics* **60**, 537 (1995).
4. J. M. Carcione, Wave propagation in anisotropic, saturated porous media: Plane wave theory and numerical simulation, *J. Acoust. Soc. Am.* **99**(5), 2655 (1996).
5. J. M. Carcione, B. Gurevich, and F. Cavallini, A generalized Biot–Gassmann model for the acoustic properties of clayley sandstones, *Geophys. Prosp.* **48**, 539 (2000).
6. J. M. Carcione and G. Quiroga-Goode, Some aspects of the physics and numerical modeling of Biot compressional waves, *J. Comput. Acoust.* **3**, 261 (1996).
7. J. M. Carcione and G. Seriani, Seismic velocities in permafrost, *Geophys. Prospect.* **46**, 441 (1998).
8. J. M. Carcione and U. Tinivella, Bottom simulating reflectors: Seismic velocities and AVO effects, *Geophysics* **65**, 54 (2000).
9. B. Fornberg, *A Practical Guide to Pseudospectral Methods* (Cambridge Univ. Press, Cambridge, UK, 1996).
10. F. Gassmann, Uber die elastizität poröser medien, *Vierteljahrsschr. Naturforsch. Ges. Zuerich* **96**, 1 (1951).
11. A. R. Gourlay, Splitting methods for time dependent partial differential equations, in *The State of the Art in Numerical Analysis*, edited by D. Jacobs (Academic Press, San Diego, 1977), p. 757.
12. B. Gurevich, O. Kelder, and D. M. J. Smeulders, Validation of the slow compressional wave in porous media: Comparison of experiments and numerical simulations, *Transport in Porous Media* **36**, 149 (1999).
13. J. Hudson, *Surface Science, an Introduction* (Butterworth-Heinemann, Boston, 1992).
14. M. K. Jain, *Numerical Solutions of Partial Differential Equations* (Wiley Eastern, New Delhi, 1984).

15. D. L. Johnson, Recent developments in the acoustic properties of porous media, in *Frontiers in Physical Acoustics*, in *Proceedings of the International School of Physics "Enrico Fermi," Course 93*, edited by D. Sette (North-Holland, Amsterdam, 1986), p. 255.
16. T. Klimentos and C. McCann, Why is the Biot slow compressional wave not observed in real rocks? *Geophysics* **12**, 1605 (1988).
17. P. Leclaire, F. Cohen-Ténoudji, and J. Aguirre-Puente, Extension of Biot's theory of wave propagation to frozen porous media, *J. Acoust. Soc. Am.* **96**, 3753 (1994).
18. P. Leclaire, F. Cohen-Ténoudji, and J. Aguirre-Puente, Observation of two longitudinal and two transverse waves in a frozen porous medium, *J. Acoust. Soc. Am.* **97**, 2052 (1995).
19. S. Mochizuki, Attenuation in partially saturated rocks, *J. Geophys. Res.* **87**, 8598 (1982).
20. W. F. Murphy, K. W. Winkler, and R. L. Kleinberg, Acoustic relaxation in sedimentary rocks: Dependence on grain contacts and fluid saturation, *Geophysics* **51**, 757 (1986).
21. W. L. Pilant, *Elastic Waves in the Earth* (Elsevier, Amsterdam, 1979).
22. E. J. Putzer, Avoiding the Jordan canonical form in the discussion of linear systems with constant coefficients, *Am. Math. Monthly* **73**, 2 (1966).
23. R. D. Stoll and G. M. Bryan, Wave attenuation in saturated sediments, *J. Acoust. Soc. Am.* **47**(2), 1440 (1970).
24. A. Timur, Velocity of compressional waves in porous media at permafrost temperatures, *Geophysics* **33**, 584 (1968).
25. C. B. Vreugdenhil, Accuracy of product-formula algorithms, *J. Comput. Phys.* **97**, 337 (1991).
26. K. W. Winkler, Dispersion analysis of velocity and attenuation in Berea sandstone, *J. Geophys. Res.* **90**(B8), 6793 (1985).
27. R. W. Zimmerman and M. S. King, The effect of the extent of freezing on seismic velocities in unconsolidated permafrost, *Geophysics* **39**, 587 (1986).